*Geophys. J. Int.* (2003) **154,** 224–229

RESEARCH NOTE

# Pressure- and temperature-dependent thermal expansivity and the effect on mantle convection and surface observables

Harro Schmeling, Gabriele Marquart* and Thomas Ruedas

*Institute of Meteorology and Geophysics, J. W. Goethe University Frankfurt, Feldbergstr.* 47, D-60323 *Frankfurt am Main, Germany.*
*E-mail: schmeling@geophysik.uni-frankfurt.de*

Accepted 2003 March 5. Received 2002 December 2; in original form 2002 April 3



## SUMMARY

In most mantle convection studies with variable thermal expansivity only the pressure dependence is considered. Here we investigate the effect of temperature- and/or pressure-dependent thermal expansivity $\alpha$ on the distribution of buoyancy forces in mantle convection. Thermal expansivity is calculated for the dominant upper-mantle mineral, forsterite, and a map of its dependence on $T$ and $p$ is given. By studying simple 2-D steady-state constant-viscosity convection and comparing cases with constant $\alpha$, $\alpha(p)$, $\alpha(T)$ and $\alpha(p, T)$ we find that at mantle temperatures the pressure dependence of $\alpha$ is important. For the lithosphere the dependence of $\alpha$ on temperature dominates, since the temperature dependence of $\alpha$ is much stronger in the low-pressure regime. Also dynamic topography changes considerably (up to 15 per cent) if $\alpha$ is $T$- and $p$-dependent compared with a constant or only $p$-dependent case. Scaling laws for the Nusselt number and the rms velocity are obtained. They differ from the constant-$\alpha$ case by at most 12 per cent if an effective Rayleigh number based on the spatial average of $\alpha$ is used.

**Key words:** mantle convection, seafloor topography, thermal expansivity.

## 1 INTRODUCTION

Thermal convection in the Earth's mantle is driven by buoyancy forces due to lateral variations in temperature leading to variations in mantle rock densities. The relation between changes in density and temperature is given by the thermal expansivity $\alpha$ of the rock material. However, the thermal expansivity is a function of temperature and pressure itself. Thus, the buoyancy forces in mantle convection are not only a function of the local temperature but also of the local value of the thermal expansivity. Despite the fact that this is basic physical knowledge, a constant $\alpha$ has been assumed in the majority of numerical models of mantle convection. In several models a depth- (i.e. pressure-) dependent $\alpha$ was assumed (e.g. Hansen *et al.* 1991, 1993; Hansen & Yuen 1994) resulting in a considerable cooling of the interior of the convection cell compared with a model with constant $\alpha$. To our knowledge a fully temperature- and pressure-dependent $\alpha$ was used in a work by Ita & King (1994) based on a Birch–Murnaghan equation of state to study the mass flux through the endothermic spinel–perovskite phase boundary in the mantle. In this work the authors tried to model the mantle behaviour as realistically as possible by invoking variable viscosity, phase boundaries and anelastic compressibility. In our variable-$\alpha$ approach we keep the model as simple as possible to investigate and understand more clearly the physics and the changes in buoyancy due to a more realistic pressure- and temperature-dependent $\alpha$. We first investigate the effects of pressure and temperature separately and then in combination. Furthermore, we also compare surface topography and geoid anomalies for the three cases to equivalent models with constant $\alpha$. This allows us to judge whether convection models used to explain such surface variables might require a realistic $\alpha$.

*Now at: Space Research Organization Netherlands & University of Utrecht, Post box 80021, 3508 TA Utrecht, the Netherlands.

## 2 THE THERMAL EXPANSIVITY

The temperature and pressure dependence of $\alpha$ may be described by the Anderson–Grüneisen parameter $\delta_T$,

$$\alpha(p, T) = \alpha_0(T)\left[\frac{V(p, T)}{V_0(T)}\right]^{\delta_T}, \tag{1}$$

where $V$ is the volume at pressure $p$ and temperature $T$, and $V_0$ is the volume at zero pressure (e.g. Fei 1995). Compression is calculated using the third-order Birch–Murnaghan equation of state, which can be approximated for the upper 1000 km of the Earth's mantle by

$$\frac{V(p, T)}{V_0(T)} = \left\{1 + \frac{2}{C}\left[-\frac{1}{2} + \sqrt{\frac{1}{4} + \frac{pC}{3K_{T_0}(T)}}\right]\right\}^{-3/2}, \tag{2}$$

where $C = 5 - \frac{3}{2}(4 - K'_{T_0})$ (see the Appendix). $K_{T_0}$ is the isothermal bulk modulus at zero pressure and $K'_{T_0}$ its pressure derivative. We use $\delta_T = 5.5$ and $K'_{T_0} = 5.37$ for forsterite (Fei 1995). For $\alpha_0(T)$ we used a law of the form (Fei 1995)

$$\alpha_0 = a_0 + a_1 T + a_2 T^{-2} \tag{3}$$

and the values for forsterite

$$a_0 = 3.034 \times 10^{-5}\ \mathrm{K}^{-1} \qquad a_1 = 7.422 \times 10^{-9}\ \mathrm{K}^{-2}$$

$$a_2 = -0.5381\ \mathrm{K}.$$

This leads to values for $\alpha_0$ of $2.514 \times 10^{-5}$ K$^{-1}$ at 273 K and of $4.33 \times 10^{-5}$ K$^{-1}$ at 1773 K. For the dependence of the bulk modulus on temperature we used a linear relation (Anderson & Isaak 1995)

$$K_{T_0}(T) = b_0 + b_1 T \tag{4}$$

with the values for

$$b_0 = 1.345 \times 10^{11}\ \mathrm{Pa} \qquad b_1 = -2.23 \times 10^{7}\ \frac{\mathrm{Pa}}{\mathrm{K}}.$$

The dependence of $\alpha$ on temperature and pressure is shown on a map in Fig. 1. The thermal expansivity increases with temperature and decreases with pressure. However, at low pressure the temperature effect is much stronger than at high pressure, and the variation of $\alpha$ is strongest in the upper 150 km. Thus, the buoyancy effect in the lithosphere is expected to be different for the upwelling and downwelling branch of the convective flow. It should be noted that we have not included the effect of phase changes. The expansivity of the high-pressure phase of forsterite, $\gamma$-spinel, is even smaller and has a weaker temperature dependence compared with forsterite at the same pressure (Saxena *et al.* 1993; Fei 1995). Thus, in our one-phase forsterite model we overestimate buoyancy within the transition zone by approximately 15–25 per cent. This error is still small compared with the overall temperature- and depth-related variations of $\alpha$ within the upper 660 km of the mantle.

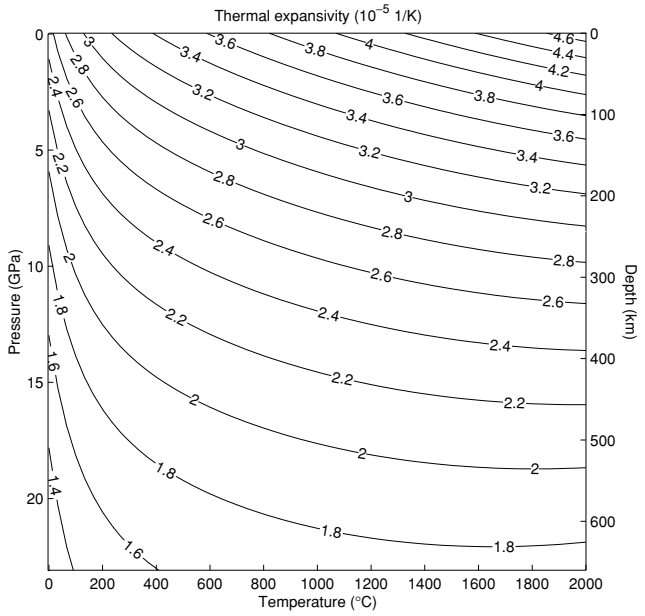


**Figure 1.** Depth- and temperature-dependent values for the thermal expansivity $\alpha$ for mantle rocks (forsterite) based on eqs (1)–(4).

**Table 1.** Numerical values of the parameters used in this study.

| Parameter | Symbol | Value |
|---|---|---|
| Height of model | $h$ | 660 km |
| Reference mantle density | $\rho_0$ | 3500 kg m$^{-3}$ |
| Gravity acceleration | $g$ | 10 m s$^{-2}$ |
| Thermal diffusivity | $\kappa$ | $10^{-6}$ m$^2$ s$^{-1}$ |
| Viscosity | $\mu$ | $10^{21}$, $3 \times 10^{21}$, $10^{22}$ Pa s |
| Scaling temperature difference | $\Delta T$ | 2000 °C |
| Scaling Rayleigh number | $Ra_{\mathrm{sc}}$ | 48 299, 160 997, 482 993 |
| Scaling thermal expansivity | $\alpha_{\mathrm{sc}}$ | $2.4 \times 10^{-5}$ K$^{-1}$ |

## 3 NUMERICAL METHOD

In the numerical formulation we have solved the Navier–Stokes and the heat transport equation in a Boussinesq approximation in the 2-D Cartesian geometry for an aspect ratio of 1 and for constant viscosity. This simple setup allows us to extract the effect of $\alpha$ on the driving (or retarding) buoyancy forces in the system. The numerical values of all parameters are given in Table 1. The scaling Rayleigh number was varied in a range resulting in an effective Rayleigh number between approximately $4 \times 10^4$ and $8 \times 10^5$.

### *Model equations*

The numerical formulation was based on solving the isoviscous Navier–Stokes, the heat transport and the mass conservation equations in 2-D Cartesian coordinates. The equations are in non-dimensionalized notation:

$$0 = -\nabla p' + \nabla^2 \mathbf{u}' - Ra_{\mathrm{sc}} \frac{\alpha(p', T')}{\alpha_{\mathrm{sc}}} T' \mathbf{e}_z \tag{5}$$

$$\frac{\partial T'}{\partial t'} = \nabla^2 T' - \mathbf{u}' \cdot \nabla T' \tag{6}$$

$$0 = \nabla \cdot \mathbf{u}' \tag{7}$$

where $p'$ is pressure, $\mathbf{u}'$ is the flow velocity, $T'$ is temperature and $t'$ is time. The primes indicate the non-dimensional variables. The scaling Rayleigh number $Ra_{\mathrm{sc}}$ is given by $(\rho_0 g \alpha_{\mathrm{sc}} \Delta T h^3)/(\kappa \mu)$. The effective Rayleigh number is obtained by inserting the spatially averaged $\alpha$ into the formula for $Ra$.

The Navier–Stokes equation was solved for primitive variables (flow velocity and pressure) using a spectral approach in the horizontal and FD in the vertical direction and the heat transport equation with second-order FD in all directions. We used free-slip boundary conditions and a constant temperature at the upper and lower side. The models consisted of 128 spectral modes in the horizontal and 120 grid points in the vertical direction. Time stepping was performed by an explicit FD scheme with dynamic time step adjustment.

**Table 2.** Mean $\alpha$, Nusselt number $Nu$, non-dimensional root-mean-square velocity $v'_{\mathrm{rms}}$, and non-dimensional mean temperature $T'$ for models with $Ra_{\mathrm{sc}} = 48\,299.33$.

| Model | $\alpha$ law | Mean $\alpha$ (1/K) | $v'_{\mathrm{rms}}$ | $Nu$ | Mean $T'$ |
|---|---|---|---|---|---|
| Mod1 | constant | $2.4000 \times 10^{-5}$ | 120.840 | 8.250 | 0.5 |
| Mod2 | $\alpha(p)$ | $2.1204 \times 10^{-5}$ | 111.034 | 7.950 | 0.48057 |
| Mod2a | constant | $2.1204 \times 10^{-5}$ | 111.830 | 7.980 | 0.5 |
| Mod3 | $\alpha(T)$ | $3.9394 \times 10^{-5}$ | 187.515 | 10.377 | 0.5025 |
| Mod3a | constant | $3.9394 \times 10^{-5}$ | 166.560 | 9.770 | 0.5 |
| Mod4 | $\alpha(p, T)$ | $2.5060 \times 10^{-5}$ | 133.110 | 8.705 | 0.4739 |
| Mod4a | constant | $2.5060 \times 10^{-5}$ | 124.510 | 8.425 | 0.5 |

To verify our results we have also calculated the root-mean-square velocities and Nusselt number with an entirely different code based on a 2-D streamfunction formulation and compared the results of the two codes, and all values agreed within 0.25 per cent. The accuracy of the global quantities in Table 2 and Fig. 4 (later) is significantly higher (∼last but one digit given), as these values were obtained from runs with various grid resolutions, then being extrapolated to an infinitely fine grid.

To estimate and visualize the distribution of buoyancy forces in the convection cell and especially in the thermal boundary layers we define a pressure- and temperature-dependent buoyancy parameter

$$b = \frac{\alpha}{\alpha_{sc}} \left( T' - \frac{1}{2} \right). \tag{8}$$

## 4 RESULTS AND DISCUSSION

In the following cases we compare models with variable $\alpha$ to others with constant $\alpha$. The $\alpha(T)$ case was obtained by setting $p = 0$ GPa

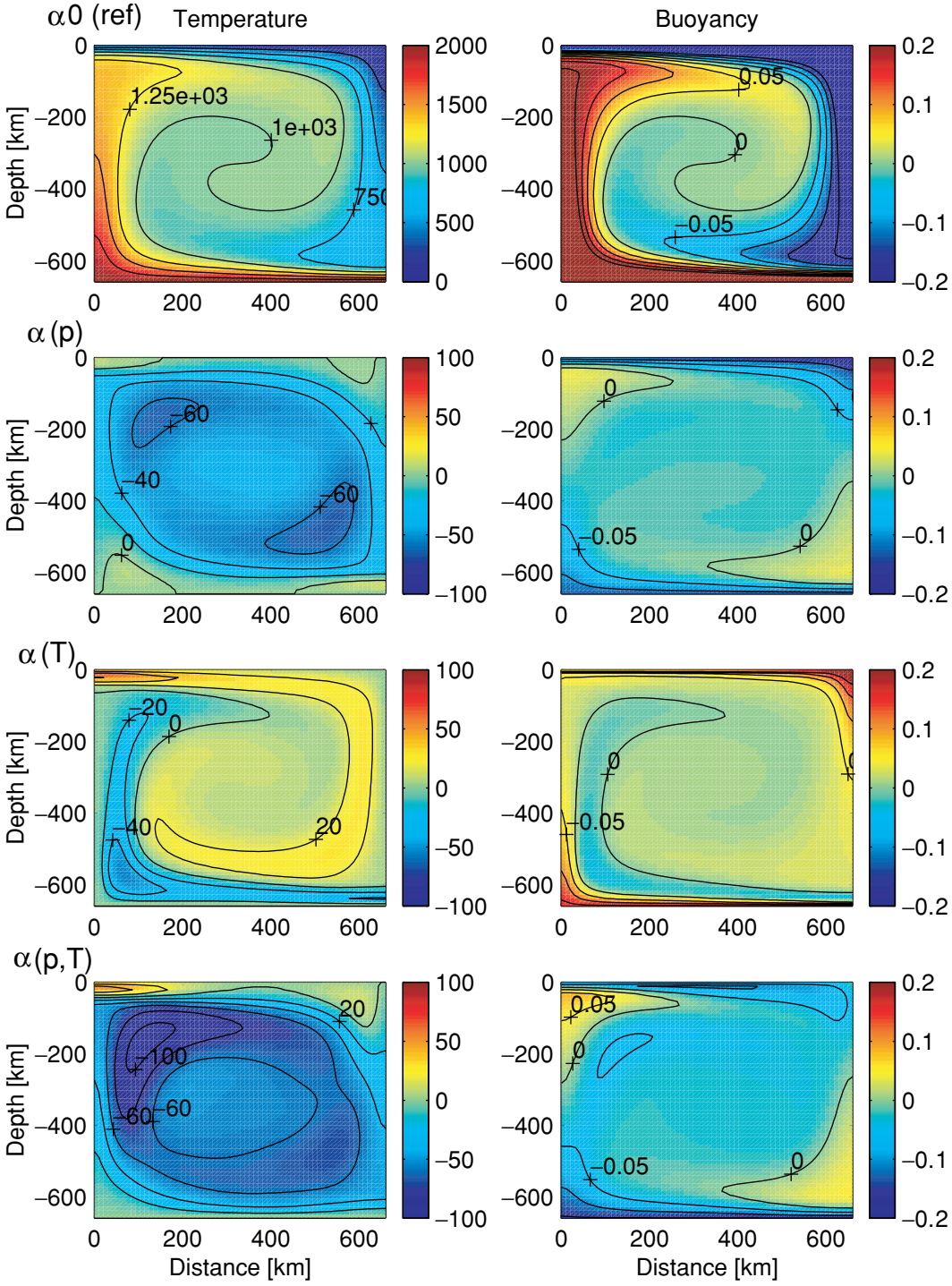


**Figure 2.** Temperature and buoyancy field for the numerical models. (a) Reference case with constant $\alpha$. (b)–(d) Cases with variable $\alpha$, here the temperature and buoyancy differences from models with constant $\alpha$ but the same Rayleigh numbers are shown.

in eqs (1)–(4); for the $\alpha(p)$ case, we set $\alpha = a_0$ and $K_{T_0} = b_0$ in eqs (3) and (4), respectively, which corresponds to $T \approx 420$ K. To ensure that the models are comparable we used the unweighted mean $\alpha$ of the variable-$\alpha$ models as the constant $\alpha$ in the corresponding models for comparison, which means that the models have the same effective Rayleigh number and similar values for the root-mean-square velocity and Nusselt number.

To show the effects of a variable $\alpha$, we define the difference of the buoyancy parameters

$$\Delta b = b(\alpha_{\text{variable}}) - b(\alpha_{\text{constant}}), \tag{9}$$

where we scaled the $b$ values with the same $\alpha_{\text{sc}}$. We first show the results of the models with the lowest scaling Rayleigh number (Table 2) in detail and then discuss the scaling laws for variable $Ra$.

The results for $Ra_{\text{sc}} = 48\,299$ are summarized in Table 2 and combined in Fig. 2; all models are in the steady state. The left-hand column of Fig. 2 gives the temperature and the right-hand column gives the buoyancy field.

The model in the upper row is the reference model for constant $\alpha$. The buoyancy field, as defined by eq. (8), is directly proportional to $T$. We see the typical symmetric temperature field for symmetric boundary conditions and aspect ratio 1. The values of the $b$ field range from 0.5 to $-0.5$.

For the models of rows 2–4 in Fig. 2, the difference in temperature and buoyancy compared with their respective reference models as defined by eq. (8) are shown. For only pressure-dependent $\alpha$ (Fig. 2, second row) the interior of the convection cell is about 50 °C cooler than the reference model. The buoyancy at the upwelling side is stronger at shallower depth and weaker in deeper parts and vice versa at the downwelling side. In other words, the driving buoyancy forces are enhanced near the top and retarded near the bottom. The cold thermal boundary layer has a larger horizontal velocity, which leads to a more effective cooling of the cell interior (in agreement with previous studies).

For the $T$-dependent $\alpha$ (Fig. 2, third row) all thermal boundary layers and the rising and sinking branches of the convection cell show considerable thinning, most pronounced just above the upwelling where a 55 °C increase in temperature is found at shallow depth. Both in the upwelling and the downwelling branch buoyancy reaches higher positive values than in the reference model. This leads to an additional driving force for the upwelling but a retardation for the downwelling and thus to an asymmetry in the two convection branches. For temperature-dependent $\alpha$, flow is generally fastest, as can be seen from the $v_{\text{rms}}$ in Table 2.

The combination of both effects, pressure and temperature dependence (Fig. 2, fourth row), is not a simple superposition. In general, the figure looks rather similar to the case of $\alpha(p)$, but the temperature of the interior of the cell is reduced even more. In the uppermost lithosphere, above the upwelling, the temperature is increased by about 50 °C. This part of the lithosphere is characterized by low pressure and high temperatures and is related to that part of the $\alpha$ map in Fig. 1 where we have the strongest variations.

The variations of driving and retarding forces along a depth profile in the centre of the up- and downwellings (at the sides of the domain) are shown in Fig. 3 for all three cases with variable $\alpha$. For the case of only temperature-dependent $\alpha$ an additional driving force acts along the entire upwelling and a retarding force along the downwelling. The overall effect of a ($p$, $T$)-dependent $\alpha$ is clearly seen: a rising plume is subjected to increasing buoyancy as the material rises. This makes plumes stronger and narrower upon rise. This has already been noticed before (Leitch *et al.* 1991), but here we show that a $T$-dependent $\alpha$ enhances this effect. On

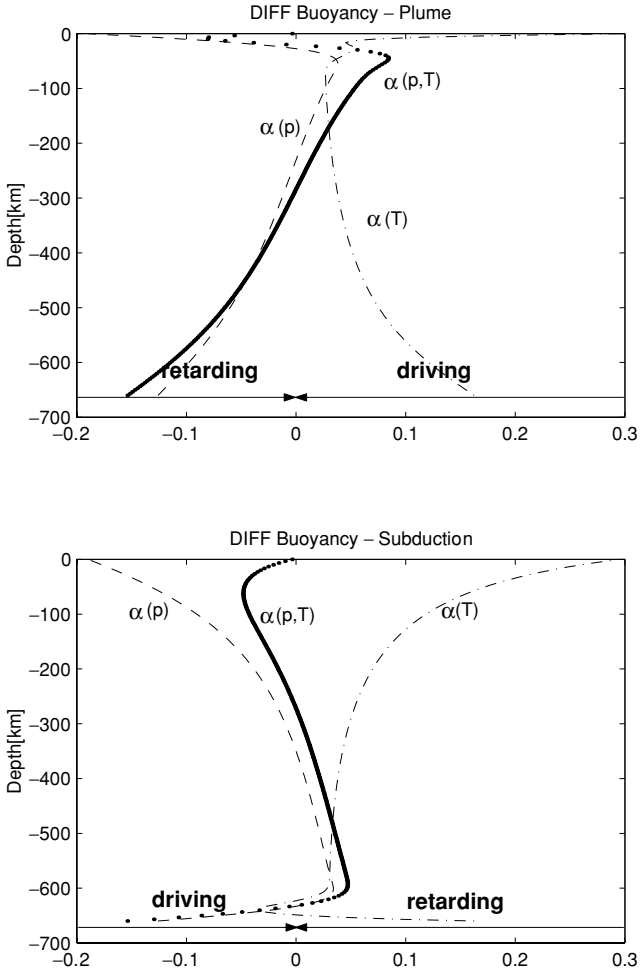


**Figure 3.** Differences in buoyancy between models with constant $\alpha$ and variable $\alpha$ versus depth for the upwelling (a) and downwelling (b) branch of the convection cell.

the other hand, downwellings experience stronger retarding forces due to an additional $T$ dependence. Taking these facts together, the combined ($p$, $T$) dependence favours narrow plumes and widens downwellings.

Dynamic topography and geoid undulations are a direct consequence of thermally induced density variations. Since the temperature field is affected by a variable $\alpha$, changes in dynamic topography and geoid will occur. We have calculated dynamic topography and geoid for all cases and show in Fig. 4 the difference between the models with variable and constant $\alpha$, scaled by the values of the reference model, respectively. The topography of the surface and bottom boundaries was calculated by equating the vertical tractions with the density jump at the boundaries times $g$ times topography. The geoid is calculated by including the mass anomalies due to deflected upper and lower boundaries and density variations due to temperature. For the cases where $\alpha$ depends on pressure or temperature only, the difference in topography compared with the reference model is of the order of 5–8 per cent, but for the case of $\alpha(p, T)$ its maximum deviation is about 15 per cent. Furthermore, not only the maximum amplitude, but also the slope of topography away from the upwelling (spreading ridge) and the topography related to the downwelling (trench) is different. Since the geoid (at least in isoviscous models) is directly related to topography, we also find the same observations for geoid undulation (Fig. 4b).

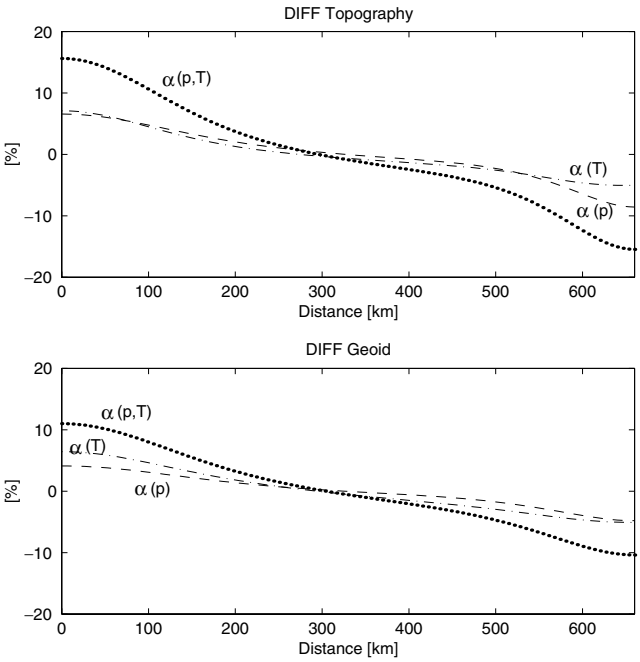


**Figure 4.** Differences in dynamic topography (a) and geoid anomaly (b) for models with constant $\alpha$ and variable $\alpha$ along the surface of the model, normalized by the values of the constant-$\alpha$ case.

We have increased the scaling Rayleigh number of the models to study the scaling laws for variable-$\alpha$ convection. The results are shown in Fig. 5. On the abscissas we plot the decadic logarithm of the effective Rayleigh number. As shown in Figs 5(a) and (b), the root-mean-square velocities $v_{\rm rms}$ and the Nusselt number $Nu$ closely follow the scaling laws $v_{\rm rms} \sim Ra_{\rm eff}^{\beta_v}$ and $Nu \sim Ra_{\rm eff}^{\beta_{Nu}}$. The $\beta$ values are very similar, ranging from 0.6341 to 0.6379 for $v_{\rm rms}$ and from 0.3201 to 0.3379 for $Nu$ for the different cases. While the scaling laws for the $\alpha =$ constant and the $\alpha(p)$ cases are virtually identical, the temperature dependence of $\alpha$ leads to slightly more vigorous convection. For same $Ra_{\rm eff}$, the rms velocities of the $T$-dependent cases are higher, namely 12 per cent for the $\alpha(T)$ case and 7 per cent for the $\alpha(p, T)$ case. A similar result, but with a reduced magnitude, is found for $Nu$. As the $T$ dependence of the $\alpha(p, T)$ case is generally less than the $T$ dependence of the $\alpha(p = 0, T)$ case (*cf.* Fig. 1), the increase in vigour is less for the $\alpha(p, T)$ case compared with the $\alpha(T)$ case.

Figs 5(c) and (d) show the mean $\alpha$ and the mean temperature for the different cases. While the $\alpha(T)$ case has a slightly higher mean temperature, the dependence of $\alpha$ on both $p$ and $T$ gives the strongest decrease of the mean temperature, even stronger than the $p$ dependence alone. This counterintuitive effect can be explained by the specific $p$ and $T$ dependence of $\alpha$ (Fig. 1): as $T$ increases, the $p$ dependence becomes even stronger. The associated decrease in the mean temperature outpaces the increase due to the $T$ dependence. At high $Ra$ the mean temperature no longer depends on $Ra$.

A variable $\alpha$ also influences adiabatic heating/cooling. For compressible convection, the temperature dependence of $\alpha$ is expected to increase the adiabatic gradient within upwelling plumes by about 10–30 per cent compared with the downwelling. In any way, as we consider upper-mantle convection only, adiabatic effects are of minor importance, and so are the related effects of a variable $\alpha$.

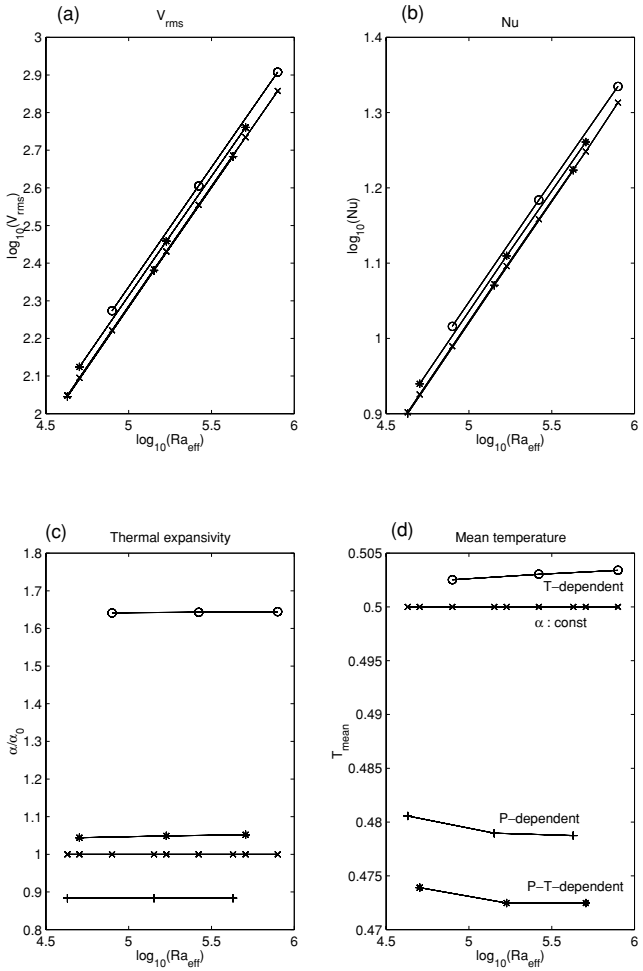


**Figure 5.** $v_{\rm rms}$, $Nu$, mean $\alpha$ and the mean temperature as a function of the effective Rayleigh number. The meaning of the line symbols is the same in every figure, and is explained in (d).

## 5 CONCLUSION

It should be noted that our models are highly simplified, as they are intended to extract and isolate the effect of a variable $\alpha$ only. As mentioned above, phase changes within the upper 660 km will lead to somewhat different $\alpha$ values, but the general behaviour within the transition zone is expected to be the same. Other effects such as variable viscosity, plate-like behaviour, compressibility or including lower-mantle phases might, however, change our findings and should be left for future studies.

From our simple modelling we draw the following conclusions: only considering the pressure effect on $\alpha$ in modelling of mantle convection is a good approximation for the temperature field and flow structure in the large-scale mantle. Allowing additionally for $T$ dependence seems to make plumes stronger and to retard slabs.

If the lithosphere and/or dynamic topography is of particular interest, then a dependence of $\alpha$ on temperature and pressure is more appropriate and considerably larger amplitudes are predicted compared with the constant-$\alpha$ or only $p$-dependent case.

Scaling laws for the Nusselt number and the rms velocities are obtained as a function of the Rayleigh number. The cases for variable $\alpha$ have the same exponents in the $Ra^{\beta}$ scaling laws as for constant $\alpha$, if an effective Rayleigh number based on the spatial average of $\alpha$ is taken. With such scaling laws the absolute $Nu$ and $v_{\rm rms}$ values differ from the constant-$\alpha$ values by at most 12 per cent.

## ACKNOWLEDGMENTS

This study was partially supported by DFG research grants Ja 258/34-2 and Schm 872/6-2 to GM and TR. We also thank two anonymous reviewers and the editor for their thoughtful and constructive reviews.

## REFERENCES

Anderson, O.L. & Isaak, D., 1995. Elastic constants of mantle minerals at high temperature, in *Mineral Physics & Crystallography—a Handbook of Physical Constants,* Vol. 2, pp. 64–97, ed. Ahrens, T.J., AGU Reference Shelf, AGU, Washington.

Fei, Y., 1995. Thermal expansion, in *Mineral Physics & Crystallography—a Handbook of Physical Constants,* Vol. 2, pp. 283–291, ed. Ahrens, T.J., AGU Reference Shelf, AGU, Washington.

Hansen, U. & Yuen, D.A., 1994. Effects of depth-dependent thermal expansivity on the interaction of thermal–chemical plumes with a compositional boundary, *Phys. Earth planet. Inter.,* **86,** 205–221.

Hansen, U., Yuen, D.A. & Kroening, S.E., 1991. Effects of depth-dependent thermal expansivity on mantle circulations and lateral thermal anomalies, *Geophys. Res. Lett.,* **18,** 1261–1264.

Hansen, U., Yuen, D.A., Kroening, S.E. & Larsen, T.B., 1993. Dynamical consequences of depth-dependent thermal expansivity and viscosity on mantle circulations and thermal structure, *Phys. Earth planet. Inter.,* **77,** 201–223.

Ita, J. & King, S.D., 1994. Sensivity of convection with an endothermic phase change to the form of governing equations, initial conditions, boundary conditions, and equation of state, *J. geophys. Res.,* **99,** 15 919–15 938.

Leitch, A.M., Yuen, D.A. & Sewell, G., 1991. Mantle convection with internal-heating and pressure-dependent thermal expansivity, *Earth planet. Sci. Lett.,* **102,** 213–232.

Saxena, S.K., Chatterjee, N., Fei, Y. & Shen, G., 1993. *Thermodynamic Data on Oxides and Silicates,* Springer, Berlin.

## APPENDIX: DERIVATION OF EQ. (2)

Here we give the derivation of eq. (2). The third-order Birch–Murnaghan equation

$$p = 3f(1+2f)^{5/2}K_{T_0}\left[1-\frac{3}{2}(4-K'_{T_0})f\right] \tag{A1}$$

is linearized to

$$p = 3fK_{T_0}\left\{1+\left[5-\frac{3}{2}(4-K'_{T_0})\right]f+\cdots\right\}. \tag{A2}$$

Here $f$ is the compression

$$f = \frac{1}{2}\left[\left(\frac{V_0}{V(p)}\right)^{2/3}-1\right]. \tag{A3}$$

Truncation of eq. (A2) after the linear term in the braces, solving for $f$, inserting $f$ into eq. (A3) and solving for $V(p)/V_0$ gives eq. (2).